Numerical Simulation of High Electron Mobility Transistors based on the Spectral Element Method

Feng Li [1], Qing H. Liu [2], and David P. Klemer [3]

[1] Department of Electrical and Computer Engineering
University of Idaho, Moscow, ID 83844, USA
fengli@uidaho.edu

[2] Department of Electrical and Computer Engineering
Duke University, Durham, NC 27708, USA
qhliu@ee.duke.edu

[3] K2 BioMicrosystems, LLC, Geneva, IL 60134, USA
david.klemer@k2biomicrosystems.com

Abstract ─ The spectral element method (SEM) is implemented for the numerical simulation of high electron mobility transistors (HEMTs) through a self-consistent solution of the Schrödinger-Poisson equations. The electron conduction band structure and electron density distribution are calculated and plotted, and results compared to those based on methods utilizing a finite-difference approach. Simulation accuracy and efficiency are analyzed and compared with traditional finite difference method (FDM). DC current-voltage (I-V) characteristics for the HEMT structure are simulated, based on a quasi-2D current model. The SEM approach offers advantages in speed and efficiency over FDM, while yielding results which conform well to reported experimental results. These advantages are particularly important for compound heterojunction devices with complex material profiles, for which FDM methods may be inefficient and computationally slow.

Index Terms ─ Heterojunction, Schrödinger equation, spectral element method, transistor.

I. INTRODUCTION

High Electron Mobility Transistors (HEMTs) – also referred to as modulation-doped FETs (MODFETs), or heterostructure FETs (HFETs) – are field-effect transistors which utilize a channel region formed by a heterojunction of (typically III-V) materials having different band gaps, in contrast to the conventional MOSFET channel formed as a three-dimensional region of doped semiconductor. The characteristics of the HEMT two-dimensional electron gas (2DEG) within the channel are typically studied by solving the Poisson-Schrödinger equations in a self-consistent matter, using various techniques such as the finite difference method [1], finite element method [2], and multigrid method [3], among others. HEMTs and related heterojunction solid-state devices can have highly complex material profiles with very small dimensions (on the scale of angstroms); accordingly, traditional numerical methods may be numerically inefficient and computationally slow, limiting their usefulness in device/circuit design and analysis applications.

The spectral element method (SEM) is a high-order finite element method which combines the advantages of the finite element method and the spectral method, resulting in computational speed advantages – by two to three orders of magnitude – when compared to conventional finite difference methods [4]. Furthermore, application of the spectral element method can result in high accuracy in numerical simulations with reasonable computational effort.

Our present research suggests that, to date, few efforts have been made to apply the spectral element method to the simulation of widely-used semiconductor devices such as the HEMT device. In this work we develop a spectral element method approach for the simulation of the HEMT structure. Although the implementation of the SEM is more complex than that of the finite difference method, we demonstrate that improvements in computational accuracy and efficiency are highly significant. This will be illustrated through comparison with computational results using the finite difference method and analysis of relative L_2 errors, (i.e., the root mean square of the error components). In addition, a quasi-two-dimensional scheme is used to study current-voltage characteristics of the HEMT device model in the triode region, based on the electron density distribution calculated from the Schrödinger-Poisson equations describing the HEMT structure,

Submitted On: November 3, 2015
Accepted On: August 18, 2016

demonstrating the further advantage of the SEM approach for device/circuit modeling and analysis.

II. THE SCHRÖDINGER-POISSON EQUATIONS

Given the idealized two-dimensional nature of the 2DEG, a quantum mechanical approach must be incorporated into the simulation in order to accurately represent carrier motion. Accordingly, the one-dimensional, single-electron, time-independent Schrödinger equation (TISE) applies:

$$-\frac{\hbar^2}{2}\frac{d}{dx}\left(\frac{1}{m^*(x)}\frac{d}{dx}\right)\psi(x)+V(x)\psi(x)=E\psi(x), \quad (1)$$

where ψ is the wave function, E represents energy, V is potential energy, $\hbar$ is Planck's constant over 2π, and m^* is the effective mass for the electron.

As is typical in semiconductor device modeling, we assume that permittivity is independent of time, and that polarization due to mechanical forces is negligible. Accordingly, the one dimensional Poisson equation is written as:

$$\frac{d}{dx}\left(\epsilon_0\epsilon_r(x)\frac{d}{dx}\right)\phi(x)=-q[N_D^+(x)-n(x)]=-\rho(x), \quad (2)$$

where ϵ_r is the relative dielectric constant, ϵ_0 is the vacuum permittivity, ϕ is the electrostatic potential, n is the electron density distribution, and N_D^+ is the ionized donor concentration. The relationship between N_D^+ and the donor concentration N_D is given by:

$$N_D^+(x)=\frac{N_D(x)}{1+2\exp\left[\frac{E_f-(V-E_D)}{k_BT}\right]}, \quad (3)$$

where E_D is the donor energy level, k_B is Boltzmann's constant, and E_f is the energy of the Fermi level.

The electron density n includes the subband electron density n_{2D} and the bulk electron density n_{3D} [5]:

$$n=n_{2D}+n_{3D}, \quad (4)$$

and the subband electron density can be expressed as:

$$\mathrm{n_{2D}(x)}=\sum_{\mathrm{j=1}}^{\mathrm{m}}\left|\psi_{\mathrm{j}}(\mathrm{x})\right|^2\mathrm{n_j}, \quad (5)$$

where m is the number of bound states, and n_j represents the electron occupation for each state, expressed as [1]:

$$n_j=\frac{m^*kT}{\pi\hbar^2}ln\left[1+exp\left(\frac{E_f-E_j}{k_BT}\right)\right]. \quad (6)$$

The 3-D bulk electron density can be expressed as [6]:

$$n_{3D}(x)=\frac{(2m^*)^{\frac{3}{2}}}{2\pi^2\hbar^3}\int_V^\infty\frac{(E-V)^{\frac{1}{2}}dE}{1+exp\left[\frac{(E-V_f)}{k_BT}\right]}, \quad (7)$$

where the potential energy V may be related to the electrostatic potential ϕ through the equation:

$$V(x)=-q\phi(x)+\Delta E_c(x), \quad (8)$$

where ΔE_c is the conduction band offset at the heterointerface.

III. NORMALIZATION AND THE STURM-LIOUVILLE DIFFERENTIAL EQUATION

The Schrödinger equation can be normalized in one dimension as [7]:

$$\left[-\frac{1}{\pi^2}\frac{d}{d\tilde{x}}\left(\frac{1}{m_r^*(\tilde{x})}\frac{d}{d\tilde{x}}\right)+\tilde{V}(\tilde{x})\right]\psi(\tilde{x})=\tilde{E}\psi(\tilde{x}), \quad (9)$$

where $\tilde{x}=\frac{x}{d_0}$, $\tilde{V}(x)=\frac{V(x)}{E_1}=\frac{[V_h(x)-q\phi]}{E_1}$, $\tilde{E}=\frac{E}{E_1}$, $E_1=\frac{\pi^2\hbar^2}{2m^*(0)d_0^2}$, $m_r^*(\tilde{x})=m^*(x)/m^*(0)$, with d_0 a reference thickness, e.g., the AlGaAs spacer thickness in the HEMT structure.

The one dimensional Poisson equation can be normalized as:

$$\frac{d}{d\tilde{x}}\left(\epsilon_r(\tilde{x})\frac{d}{d\tilde{x}}\right)\phi(\tilde{x})=-\tilde{\rho}(\tilde{x}), \quad (10)$$

where $\epsilon_r(\tilde{x})=\frac{\epsilon_0\epsilon_r(x)}{\epsilon(0)}$ and $\tilde{\rho}(\tilde{x})=\frac{d_0^2}{\epsilon(0)}\rho(x)$.

These normalized Schrödinger and Poisson equations can be treated as special forms of the Sturm-Liouville differential equation:

$$\left[-\frac{d}{d\tilde{x}}\left(\eta(\tilde{x})\frac{d}{d\tilde{x}}\right)+\tilde{V}(\tilde{x})\right]u(\tilde{x})=\tilde{E}u(\tilde{x})+\tilde{\rho}(\tilde{x}), \quad (11)$$

which becomes the Schrödinger equation for $\tilde{\rho}(\tilde{x})=0$ and $\eta(\tilde{x})=\frac{1}{\pi^2 m_r^*(\tilde{x})}$, and the Poisson equation for $\tilde{V}(\tilde{x})=0$, $\tilde{E}=0$, and $\eta(\tilde{x})=\epsilon_r(\tilde{x})$.

Finally, multiplying the above equation by a time-independent test function v on both sides, and integrating the equation over the spatial domain Ω, a weak formulation of the Sturm-Liouville differential equation can be obtained:

$$\int_\Omega\left(\eta\frac{du}{d\tilde{x}}\right)\cdot\frac{dv}{d\tilde{x}}d\tilde{x}+\int_\Omega\tilde{V}uvd\tilde{x}=\int_\Omega\tilde{E}uvd\tilde{x}+\int_\Omega\tilde{\rho}vd\tilde{x}. \quad (12)$$

IV. DISCRETIZATION AND MATRIX FORMULATION

One characteristic of the spectral element method is adopted from the finite element method, i.e., the domain under study is divided into K elements. In implementing this division, the spatial location of any semiconductor device inhomogeneity, e.g., a material heterojunction, must be considered in order to avoid an ambiguity which occurs when different materials (e.g., AlGaAs and GaAs) appear within a single element of the numerical grid. After discretization into elements, integrations involved in the original equations may be performed individually on each element, specifically:

$$\int_{\Omega_k}\left(\eta\frac{du}{d\tilde{x}}\right)\cdot\frac{dv}{d\tilde{x}}d\tilde{x}+\int_{\Omega_k}\tilde{V}uvd\tilde{x}=\int_{\Omega_k}\tilde{E}uvd\tilde{x}+\int_{\Omega_k}\tilde{\rho}vd\tilde{x}, \quad (13)$$

for $k=1,\dots,K$.

A mathematical mapping is then implemented, and a global physical coordinate $x\in[x_k,x_{k+1}]$ for each element K is mapped into a local coordinate $\xi\in\Lambda=[-1,1]$ for the Gauss-Lobatto-Legendre (GLL) integration quadrature. The mapping function takes the form of:

$$x(\xi)=x_k+\Delta x\frac{\xi+1}{2}, \quad (14)$$

where $\Delta x=x_{k+1}-x_k$ is the length of element Ω_k, and

x_k and x_{k+1} represent respectively the left and right endpoints of element Ω_k.

As usual, this coordinate transformation requires the inclusion of the so-called Jacobian J_k within the integrand:

$$\int_{\Omega_k} f(x)dx = \int_{\Lambda} f^{(k)}(\xi)\frac{dx^{(k)}}{d\xi}d\xi = \int_{-1}^{1} f^{(k)}(\xi)J_k d\xi, \quad (15)$$

where the integrand function $f(x)$ is an arbitrary function and the superscript (k) denotes the restriction of $f(x)$ to element k. $J_k = \frac{dx^{(k)}}{d\xi} = \frac{\Delta x^{(k)}}{2}$ is the Jacobian for the k^{th} element. To perform the integration over Λ, GLL quadrature is applied, reducing the integral to a finite weighted sum:

$$\int_{\Lambda} f(\xi)\,d\xi \approx \sum_{i=0}^{N} w_i f(\xi_i), \quad (16)$$

where w_i represents the weights of the GLL quadrature.

Following domain decomposition, a GLL interpolation scheme is applied to the function u in the one-dimensional Sturm-Liouville differential equation above, applied to each element. A test function v is also defined:

$$u^{(k)}(\tilde{x}) = \sum_{j=0}^{N} u^{(k)}(\tilde{x}_j)b_j^{(k)}(\tilde{x}), \quad (17)$$

$$v_i^{(k)}(\tilde{x}) = b_i^{(k)}(\tilde{x}), \quad (18)$$

where $b_j\ (\tilde{x})$ represents the N[th]-order GLL interpolation polynomial:

$$b_j(x) = \frac{-1}{N(N+1)L_N(\tilde{x}_j)}\frac{(1-\tilde{x}^2)L_N'(\tilde{x})}{\tilde{x}-\tilde{x}_j}, \quad (19)$$

in which L_N represents the Legendre polynomial of the Nth order, and L_N' its derivative.

Finally, the Sturm-Liouville differential equation can be transformed to:

$$\sum_{j=0}^{N}\left\{u^{(k)}(\xi_j)\cdot\sum_{i=0}^{N}\sum_{l=0}^{N}\left[\frac{db_i^{(k)}(\xi_l)}{d\xi}\frac{db_j^{(k)}(\xi_l)}{d\xi}\cdot w_l^{(k)}\eta(\xi_l)\cdot\frac{1}{J_k}+\tilde{V}(\xi_l)b_i^{(k)}(\xi_l)b_j^{(k)}(\xi_l)\cdot w_l^{(k)}\eta(\xi_l)\cdot J_k\right]\right\} = \sum_{j=0}^{N}\left\{u^{(k)}(\xi_j)\cdot\sum_{i=0}^{N}\sum_{l=0}^{N}\left[\tilde{E}\cdot b_i^{(k)}(\xi_l)b_j^{(k)}(\xi_l)\cdot w_l^{(k)}\eta(\xi_l)\cdot J_k\right]\right\} + \sum_{i=0}^{N}\sum_{l=0}^{N}\left[b_i^{(k)}(\xi_l)\cdot w_l^{(k)}\tilde{\rho}(\xi_l)\cdot J_k\right], \quad (20)$$

which can be written succinctly in matrix notation as:

$$\boldsymbol{A}U = \lambda\boldsymbol{B}U + \hat{f}(\Phi). \quad (21)$$

As mentioned earlier, the Sturm-Liouville equation reduces to the Schrödinger equation for $\tilde{\rho} \equiv 0$, which can be written in the matrix form:

$$\boldsymbol{A}\Psi = \lambda\boldsymbol{B}\Psi, \quad (22)$$

where $\boldsymbol{A}$ is the stiffness matrix, $\boldsymbol{B}$ is the diagonal matrix by virtue of the quadrature, and Ψ is the wavefunction to be determined.

Since the matrix $\boldsymbol{B}$ is a diagonal matrix, equation (22) can be written as a regular eigenvalue problem, which can be solved more efficiently:

$$\tilde{\boldsymbol{A}}\tilde{\Psi} = \lambda\tilde{\Psi}, \quad (23)$$

where $\tilde{\boldsymbol{A}} = \boldsymbol{B}^{-1/2}\boldsymbol{A}\boldsymbol{B}^{-1/2}$, and $\tilde{\Psi} = \boldsymbol{B}^{1/2}\Psi$.

Similarly, the Sturm-Liouville equation reduces to the Poisson equation for $\tilde{V} = 0$ and $\tilde{E} = 0$, which can also be expressed in matrix form:

$$\boldsymbol{A}\Phi = \hat{f}(\Phi). \quad (24)$$

This equation can be solved using Newton-Raphson iteration in the usual manner:

$$\Phi^{(n+1)} = \Phi^{(n)} - \left[\boldsymbol{A} - \frac{\partial\hat{f}\left(\Phi_i^{(n)}\right)}{\partial\Phi_j}\right]^{-1}\left(\boldsymbol{A}\Phi^{(n)} - \hat{f}\left(\Phi^{(n)}\right)\right), \quad (25)$$

where the index n denotes the nth iteration.

V. BOUNDARY CONDITIONS

At this point, we consider a typical AlGaAs/GaAs HEMT structure, with the conduction band profile schematically shown in Fig. 1. When solving the Poisson equation for HEMTs, we may choose $E_f = 0$; the electrostatic potential at the gate ($x = 0$) is determined by the Schottky barrier height and the applied gate voltage: $\phi(x_0) = \phi_{ms} - V_{gate}$. At the gate ($x = 0$), $\phi(x_0) = \phi_0$, the value of the electrostatic potential applied to the HEMT gate, a function of the choice of Fermi level E_f.

Intrinsic to the derivation of the weak formulation, Neumann-type boundary conditions are naturally included for the Schrödinger equation in the spectral element method; this is a significant advantage of the SEM approach for solving the Schrödinger equation, as compared with the FDM approach. In contrast, with FDM, the process of handling Neumann-type boundary conditions for the Schrödinger equation is awkward and requires significant numerical effort.

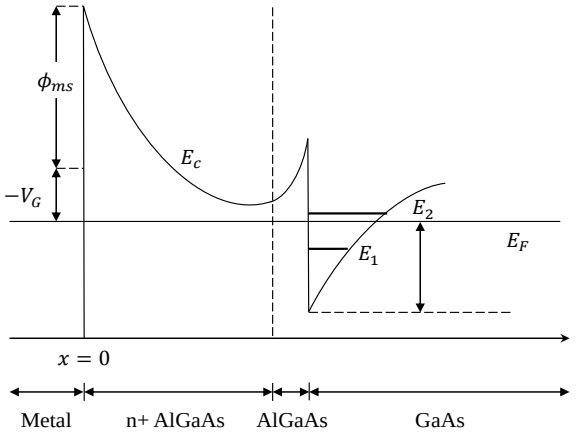

Fig. 1. Conduction band profile for a typical HEMT device.

VI. ELECTRON CONDUCTION BAND AND ELECTRON DENSITY DISTRIBUTION

The physical parameters of a typical AlGaAs/GaAs HEMT device used for numerical testing are summarized in Table 1 below. The device consists of a doped

$Al_{0.3}Ga_{0.7}As$ layer, 20 nm in depth, with a doping density of $3 \times 10^{18}/cm^3$, above an undoped $Al_{0.3}Ga_{0.7}As$ barrier (spacer) layer, 5 nm in depth, positioned above a deep (175 nm) GaAs buffer layer.

Figure 2 illustrates computational results for the electron conduction band energy and electron density distribution with no external bias, with results shown using both FDM- and SEM-based simulations.

Table 1: HEMT physical parameters used for simulation

Material	x	Thickness (Å)	Doping (/cm^3)	Relative Dielectric Constant	Effective Mass (m_0)
n+ Al_xGa_{1-x} As	0.3	200	3E+18	12.2	0.092
Al_xGa_{1-x} As	0.3	50	0	13.1	0.092
GaAs	0	1750	0	13.1	0.067

x represents the Al mole fraction for the Al_xGa_{1-x} As material; m_0 is the effective mass for electrons.

The expected quantum well at the heterojunction (x=250 Angstroms) is clearly evident, as is the accumulation of electron charge carriers (the 2DEG) in the region of the quantum well. The electron distribution "spills out" slightly into the material above the heterojunction (x < 250 Angstroms), illustrating the need for an undoped spacer layer to avoid Coulombic interactions between electrons and ionized dopant atoms. It can be seen that FDM and SEM simulations provide consistent results with regard to electron conduction band energy and electron density distribution, supporting the validity of the SEM implementation for numerical solution of the Schrödinger-Poisson equation.

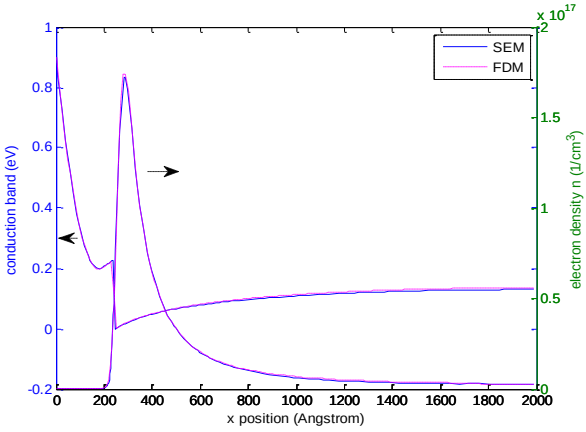

Fig. 2. Conduction band energy value and electron density distribution for the HEMT device of Table 1, calculated from SEM and FDM simulations.

VII. SIMULATION EFFICIENCY AND ACCURACY ANALYSIS

Visual comparisons of graphically plotted solutions (e.g., in Fig. 2) are qualitatively helpful, but lack quantitative rigor. One formal quantitative metric would be the rate of numerical convergence as a function of an increasing number of unknowns. The comparison of simulation time is also useful. Figure 3 shows a comparison of error as a function of simulation CPU time for FDM and SEM. It can be seen that, to reach similar accuracy, SEM is nearly 40 times faster than FDM for this one dimensional simulation.

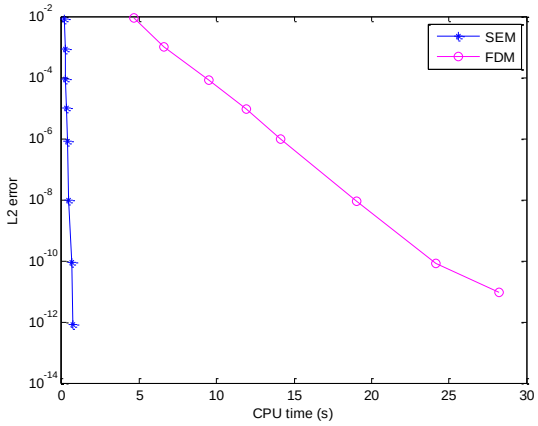

Fig. 3. Error as a function of CPU time for FDM and SEM.

Given that computational (CPU) time is directly related to the number of nodes defined for the computer simulation, we can also study L_2 errors as a function of grid size (i.e., number of nodes) in lieu of CPU time. Furthermore, instead of directly using grid size in a direction along an axis perpendicular to the device surface, the parameter number of points per wavelength (PPW) is used for normalization.

Figure 4 shows relative L_2 error for a simulated static potential computed using the FDM approach, as a function of PPW. It is apparent that L_2 error drops below approximately 0.5% if a minimum of 100 points-per-wavelength are chosen for the FDM simulation. In contrast, the SEM-based approach (with GLL order of 2) requires only 3 points-per-wavelength to achieve this level of accuracy, as shown in Fig. 5, demonstrating a significant improvement in efficiency and accuracy over the FDM approach. It is also apparent that L_2 error decreases approximately linearly with increases in PPW, as evident in the log-log graphs for both FDM- and SEM-based computational approaches.

Finally, Fig. 5 illustrates that the rate of decrease in L_2 error as a function of increasing PPW is greater for higher-order GLLs. To achieve errors in the range 0.1% to 1%, a GLL order of $N = 4$ and PPW value of 4 points per wavelength would suffice for spectral element simulations of HEMT device structures.

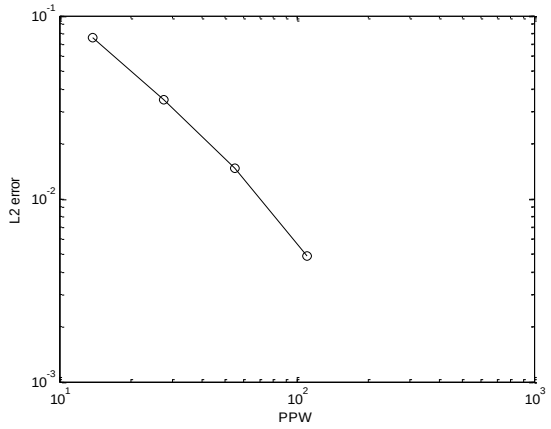

Fig. 4. Relative L_2 error in computed electrostatic potential as a function of points-per-wavelength, for FDM-based simulations.

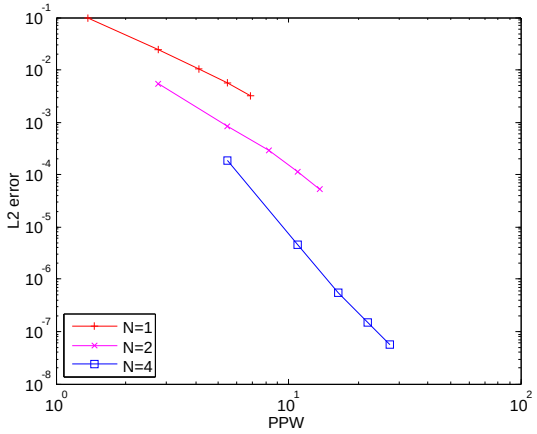

Fig. 5. L_2 error in computed electrostatic potential as a function of PPW, for SEM-based simulations having various GLL orders N (N = 1, 2 and 4).

VIII. HEMT CURRENT-VOLTAGE CHARACTERISTICS

The direct-current (DC) current-voltage (I-V) characteristics for a HEMT device can be calculated based on a quasi-two-dimensional (quasi-2D) drift-diffusion current model, using computational results of the electron density distribution [8, 9]. Figure 6 shows a schematic illustration of the quasi-2D current model which applies to the HEMT device structure under consideration.

The 2DEG sheet charge density is a function of voltage along the channel:

$$n_s(V) = \int n(V,z)dz, \tag{26}$$

and the drain current is:

$$I_D = -qWv(x)n_s. \tag{27}$$

The computation of drain current requires knowledge of the relationship between drift velocity and electric field (the v - E relationship); for increased accuracy, experimental measurements of the nonlinear v - E relationship (from [10]) are used for current calculations. Device parameters for the simulated AlGaAs/GaAs HEMT are taken from [11], specifically: gate width $W = 60\mu m$, gate length $L = 0.5\mu m$, gate metallization Ti/Pt/Au, Schottky barrier height $\phi_B = 0.58V$, Si-doped n- $Al_{0.28}Ga_{0.72}As$ layer thickness $d_{n^+} = 30nm$ with doping concentration $N_D = 1.5 \times 10^{18}/cm^3$, undoped $Al_{0.28}Ga_{0.72}As$ spacer layer thickness of $\delta d = 4\,nm$ and mole fraction $x = 0.28$. Source and drain resistances are assumed to be $R_s = R_d = 0.05\ \Omega cm$ [12, 13]. These values are highly process-dependent, thus typical values are chosen empirically here.

Based on this quasi-2D current model and knowledge of the electron density distribution (calculated from the Schrödinger-Poisson equations using the spectral element method), the current-voltage characteristics for the HEMT triode region can be determined (Fig. 7). Simulated points are shown by discrete markers in Fig. 7; the solid lines which interconnect simulation points of like gate voltage are provided for convenience in visualizing trends only. These results conform well to experimental data obtained for the triode region in Thomasian et al. [11].

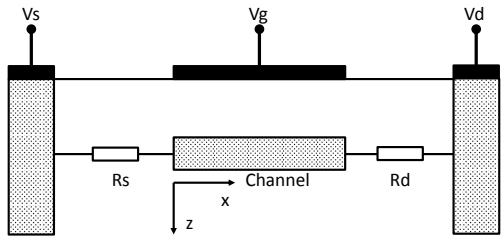

Fig. 6. A quasi-2D current model for the HEMT device.

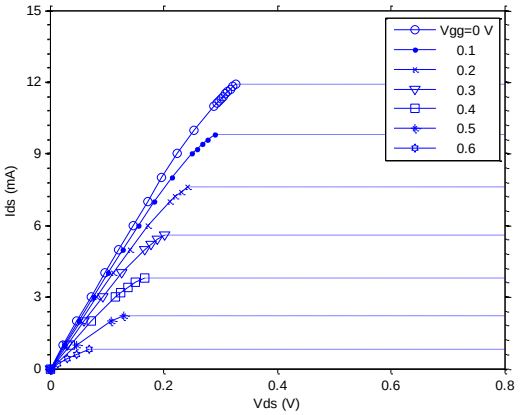

Fig. 7. I-V characteristics of an AlGaAs/GaAs HEMT.

IX. CONCLUSIONS

It is clear that implementation of the spectral element method in numerical simulations of the conduction band

structure and 2DEG electron distribution in HEMT devices offers significant advantages in numerical efficiency and relative accuracy when compared to less-complex methods, such as the finite difference method. Furthermore, results from SEM-based simulation can facilitate the determination of device terminal I-V characteristics in a much more computationally-efficient manner, as compared to traditional methods. Estimation of AC small-signal parameters from large-signal data now becomes numerically feasible given the greater computational speed associated with an SEM-based method. This can facilitate both small-signal analysis and design and nonlinear large-signal analysis. Given the increasing interest in applying heterostructure-based compound semiconductor devices to new application areas (e.g., optical, chemical, and biological sensors), the SEM-based approach demonstrated herein can permit efficient numerical design of complex device structures having novel material profiles.

REFERENCES

[1] I.-H. Tan, G. L. Snider, L. D. Chang, and E. L. Hu, "A self-consistent solution of Schrödinger-Poisson equations using a nonuniform mesh," *J. Appl. Phys.*, vol. 68, no. 8, pp. 4071-4076, Oct. 1990.

[2] S. Lapaul, A. de Lustrac, and F. Bouillault, "Solving the Poisson's and Schrödinger's equations to calculate the electron states in quantum nano-structures using the finite element method," *IEEE Trans. Magnetics*, vol. 32, no. 3, pp. 1018-1021, May 1996.

[3] E. A. B. Cole, C. M. Snowden, and T. Boettcher, "Solution of the coupled Poisson-Schrödinger equations using the multigrid method," *Int. J. Numer. Model E. L.*, vol. 10, no. 2, pp. 121-136, Mar. 1997.

[4] C. Cheng, J.-H. Lee, H. Z. Massoud, and Q. H. Liu, "3-D self-consistent Schrödinger-Poisson solver: The spectral element method," *J. Comput. Electron.*, vol. 7, no. 3, pp. 337-341, Feb. 2008.

[5] A. Abou-Elnour and K. Schuenemann, "A comparison between different numerical methods used to solve Poisson's and Schrödinger's equations in semiconductor heterostructures," *J. Appl. Phys.*, vol. 74, no. 5, pp. 3273-3276, Sep. 1993.

[6] H. C. Casey, *Devices for Integrated Circuits: Silicon and III-V Compound Semiconductors.* Wiley, 1998.

[7] Q. H. Liu, C. Cheng, and H. Z. Massoud, "The spectral grid method: a novel fast Schrödinger-equation solver for semiconductor nanodevice simulation," *IEEE Trans. Comput. Aid. Des. Integr. Circ. Syst.*, vol. 23, no. 8, pp. 1200-1208, Aug. 2004.

[8] F. Sacconi, A. Di Carlo, P. Lugli, and H. Morkoc, "Spontaneous and piezoelectric polarization effects on the output characteristics of AlGaN/GaN heterojunction modulation doped FETs," *IEEE Trans. Electron Devices*, vol. 48, no. 3, pp. 450-457, Mar. 2001.

[9] J. S. Blakemore, "Semiconducting and other major properties of gallium arsenide," *J. Appl. Phys.*, vol. 53, no. 50, pp. 123-181, Oct. 1982.

[10] A. Thomasian, A. A. Rezazadeh, and L. G. Hipwood, "Observation and mechanism of kink effect in depletion-mode AlGaAs/GaAs and AlGaas/GaInAs HEMTs," *Electron Lett.*, vol. 25, no. 5, pp. 351-353, Mar. 1989.

[11] K. A. Christianson and W. T. Anderson, "Determination of AlGaAs/GaAs HEMT parasitic resistance," *Solid State Electron.*, vol. 39, no. 12, pp. 1757-1760, Dec. 1996.

[12] K. L. Priddy, D. R. Kitchen, J. A. Grzyb, C. W. Litton, T. S. Henderson, C.-K. Peng, W. F. K. Kopp, and H. Morkoc, "Design of enhanced Schottky-barrier AlGaAs/GaAs MODFET's using highly doped p surface layers," *IEEE Trans. Electron Devices*, vol. 34, no. 2, pp. 175-180, Aug. 2005.

[13] K. L. Priddy, D. R. Kitchen, J. A. Grzyb, C. W. Litton, T. S. Henderson, C. K. Peng, W. F. K. Kopp, and H. Morkoc, "Design of enhanced Schottky-barrier AlGaAs/GaAs MODFET's using highly doped p surface layers," *IEEE Trans. Electron Device*, vol. 34, no. 2, pp. 175-180, 2005.

Feng Li received the Ph.D. degree in Electrical Engineering from the University of Wisconsin-Milwaukee in 2012, and M.S. degree in Electrical Engineering from the University of Texas at Arlington in 2004. He is currently an Assistant Professor of Electrical and Computer Engineering at University of Idaho. From 2004 to 2014, he was doing research at Duke University and University of Wisconsin-Milwaukee. His research interests include simulation, design, fabrication and characterization of III-V compound semiconductor microelectronic and optoelectronic devices.

Qing Huo Liu received the Ph.D. degree in Electrical Engineering from the University of Illinois at Urbana-Champaign, in 1989.

From January 1989 to February 1990, he was a Postdoctoral Research Scientist and Program Leader with Schlumberger-Doll Research, Ridgefield, CT. From 1996 to May 1999, he was an

Associate Professor with New Mexico State University, Since June 1999, he has been with Duke University, Durhm, NC, where he is currently a Professor of Electrical and Computer Engineering. He has authored or co-authored over 450 papers in refereed journals and conference proceedings. His research interests include computational electromagnetics and acoustics, inverse problems, geophysical subsurface sensing, biomedical imaging, electronic packaging, and the simulation of photonic devices and nanodevices.

He is a Fellow of IEEE, and a Fellow of the Acoustical Society of America. He is a member of Phi Kappa Phi and Tau Beta Pi. He is a Full Member of the U.S. National Committee, URSI commissions B and F. He is an Associate Editor for the IEEE Transactions and Geoscience and Remote Sensing. He was the recipient of the 1996 Presidential Early Career Award for Scientists and Engineers (PECASE) presented by the White House, the 1996 Early Career Research Award presented by the Environmental Protection Agency, and the 1997 CAREER Award presented by the National Science Foundation (NSF).

David P. Klemer received an M.D. degree from Columbia University, New York City, NY, in 1999, and Ph.D. degree in Electrical Engineering from The University of Michigan, Ann Arbor, MI, in 1982. His research interests are based on an interdisciplinary background in engineering and medicine, with past research activities including optical imaging at near-infrared wavelengths, microelectronic device/circuit fabrication based on Si and III-V compounds, and the design of solid-state devices and circuits for biosensing and medical diagnostics. His interests include the broad application of biomedical imaging systems, biophotonics and biomedical instrumentation to explorations of human pathophysiology, disease diagnosis and management, and physiologic monitoring in critical care environments. Klemer completed a residency in Internal Medicine at NYU Medical Center/Bellevue Hospital in New York City, and is a Diplomat of the National Board of Physicians and Surgeons.